Sensors & Actuators: A. Physical 363 (2023) 114699

Contents lists available at ScienceDirect

Sensors and Actuators: A. Physical

journal homepage: www.journals.elsevier.com/sensors-and-actuators-a-physical

Numerical simulation, fabrication, and characterization of a heating system for integration into an Organ-on-a-Chip

Gabriel M. Ferreira [a,b,c], Filipe M. Azevedo [a,b], Paulo J. Sousa [a,b], Vânia C. Pinto [a,b], Susana O. Catarino [a,b], Patrícia C. Sousa [c], Graça Minas [a,b,*]

[a] Microelectromechanical Systems Research unit (CMEMS-UMinho), School of Engineering, Campus de Azurém, University of Minho, 4800–058 Guimarães, Portugal
[b] LABBELS—Associate Laboratory, 4800–122 Braga, Portugal
[c] International Iberian nanotechnology Laboratory, INL, 4715–330 Braga, Portugal

ARTICLE INFO

Keywords:
COMSOL Multiphysics
Microfabrication
Microheater
Organ-on-a-chip
Proportional–integral–derivative controller, temperature

ABSTRACT

In an organ-on-a-chip (OoC) device, temperature control is essential for a well-controlled and human representative microenvironment. This work presents the design, numerical simulation, fabrication and characterization of three aluminium microheater geometries for temperature control into an OoC device. Two of them are circular-based, with different curvature filleting angles and different line widths, and the third is a Hilbert-based geometry. Numerical simulations in COMSOL Multiphysics were performed to evaluate the heat distribution and power consumption of each resistive microheater, by Joule effect, according to target temperature range needed: 35 ºC (physiological) to 45 ºC (hyperthermia). Those simulated microheaters were fabricated on top of a glass substrate, using standard microfabrication technologies and bonded to a polydimethylsiloxane chamber that will contain the cultured organ model. An infrared thermal camera was used for the experimental heating tests and a proportional–integral–derivative (PID) controller, implemented on a printed circuit board, was used for monitoring and controlling the chamber temperature around its target range. Despite the observed differences between the numerical and experimental power consumption, needed for reaching the target temperatures, the obtained heating distribution and the temperature variations showed a good match for all geometries. Both the numerical and experimental results of the Hilbert-based geometry showed an ellipsoidal heat distribution in the circular culture chamber, which allowed to conclude an impair in the chamber temperature uniformity. Regarding the PID controller of the heating system, it was tested for long periods of time (>12 h) without loss of performance or overheating and the results showed a variation of 0.05 ºC/s during the cooling and 0.02 ºC/s during the heating phases, with a resolution of 1 ºC for temperatures up to 42 ºC, and ~0.5 ºC for temperatures below 38 ºC. Thus, the developed numerical approach enabled to qualitatively predict the performance of different microheater geometries, allowing to optimize the heating system performance, required for integration into an OoC.

1. Introduction

Organ-on-a-chip (OoC) devices are microfluidic cell culture systems with controlled dynamic conditions that directly emulate the physical, chemical and mechanical microenvironment of cells and tissues in the human body. As a result, these devices exhibit tissue- and organ-level functions that are not found in other, more simple, *in vitro* 2D cell cultures [1,3]. Additionally, multiple organs can be integrated by linking individual OoC through microfluidic channels, with volume ratios and flow distributions that mimic the *in vivo* physiological coupling, creating *in vitro* models of human body subsystems [4]. These systems have recently emerged as viable platforms for in-depth understanding of disease mechanisms and testing novel therapies increasing their efficiency foreseen precision medicine [5,6].

The development of OoC devices requires cell culture domains, which, together with the microfluidic system, allow the 2D and 3D cell

* Corresponding author at: Microelectromechanical Systems Research unit (CMEMS-UMinho), School of Engineering, Campus de Azurém, University of Minho, 4800–058 Guimarães, Portugal.

E-mail addresses: id10786@alunos.uminho.pt (G.M. Ferreira), a68590@alunos.uminho.pt (F.M. Azevedo), psousa@dei.uminho.pt (P.J. Sousa), vpinto@dei.uminho.pt (V.C. Pinto), scatarino@dei.uminho.pt (S.O. Catarino), patricia.sousa@inl.int (P.C. Sousa), gminas@dei.uminho.pt (G. Minas).

https://doi.org/10.1016/j.sna.2023.114699
Received 22 May 2023; Received in revised form 14 September 2023; Accepted 26 September 2023
Available online 28 September 2023

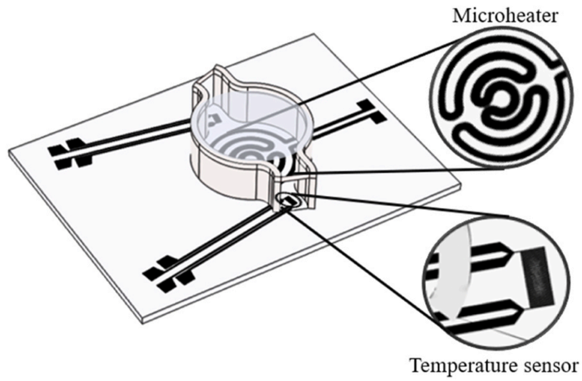

Fig. 1. Schematic representation of a microheater and temperature sensors integrated in the PDMS circular culture chamber of an OoC device.

growth if the maintenance of an adequate microenvironment for the cellular cultures is assured. Therefore, it is necessary to monitor and control several environment parameters, such as O_2 and CO_2 concentrations, pH, temperature, among others [2,7]. In particular, temperature is a critical parameter for the occurrence of physical, chemical and biological reactions in a reproducible and accurate way [5,8]. Furthermore, a stable and controlled temperature environment is essential for cells' viability growth [9]. Several technologies have been applied for heating and temperature control systems in microfluidic devices, presenting advantages and disadvantages in terms of integration, cost, heat distribution and accuracy. In some applications, a tolerance for small temperature variations is not critical for the device performance. However, in other applications, the performance may be significantly affected, such as when considering the biological activity of cells, which are extremely sensitive to slight temperature variations [10].

There are different heating solutions already available. Heating using lasers, although effective in rapidly heating very small volumes, has some restrictions in the fields of cell culture, especially because it is necessary to uniformly and continuously heat a larger volume of fluid [11,12]. Chemical heating in microfluidic applications has revealed serious challenges in sustaining heat for an extended period. Despite being a low-cost approach, constant monitoring of reagents implies the use of extra equipment, which makes this option limited [13,14]. Microwave heating is a widely used method for rapid heating of microfluids, but it requires complex and expensive equipment and the heating is not as efficient as other techniques [13,15]. Regarding electromagnetic radiation heating, although allowing uniform heating, especially in fluids, it suffers from electromagnetic interferences with the electronic circuits and other electrical sensors operation. Additionally, it also heats the fluids locally and not the entire system. Regarding Joule effect heating, it occurs when an electric current, circulating in a conductive material, causes power loss in the form of heat. It also presents some disadvantages, such as the difficulty to precisely monitor and control the generated temperature and the complex coupling between temperature and electrical field distribution [16]. However, Joule heating allows to obtain miniaturized and integrated devices, with faster and uniform heating rates and low power consumption [16]. In addition, the potential for miniaturization, combined with the ease fabrication directly on the microfluidic substrates proved to be a good solution [17,18].

Thus, herein it is presented the development of a low cost and miniaturized heating system, based on Joule effect, as well as its respective actuation and readout electronics. This system will be integrated into a microfluidic device that comprises a polydimethylsiloxane (PDMS) circular culture chamber (8 mm diameter, 3 mm height) for the organ model and two temperature sensors based on resistance temperature detectors (RTDs), for temperature measurements [5], as exemplified in Fig. 1.

The design of a such system included numerical simulations of different aluminium microheater geometries using COMSOL Multiphysics software. There are already some numerical studies reported in literature focusing on Joule heating, with focus on the phenomena of heat losses occurring in microfluidic devices [19–21]. In particular, Papadopoulos et al. (2021) studied the convective heat losses, through an heat transfer coefficient, in a static chamber of a microfluidic device, and proved the importance of including these phenomena when using numerical simulators [19]. Regarding these losses, some studies assume the heat transfer coefficient as a constant [22], while others, as Papadopoulos et al., have achieved more satisfactory results with temperature dependence models [19].

Besides the numerical losses model, the geometry of the microheater is one of the most important parameters for controlling the achieved temperature, as it directly influences heat generation and distribution. So, three geometries (two circular-based shaped and one Hilbert-based geometry) were numerically simulated in this work, to find the best geometry capable of generating heat, in a homogeneous and controlled manner, throughout the entire area of the cell culture chamber. The system requirements must be able to heat the entire volume of fluid in the system, in a target temperature range between 35 ºC and 45 ºC, in order to cover optimal cell growth temperatures, as well as hypothermia and hyperthermia situations [5,23,24]. Furthermore, in an OoC system, the temperature in the microfluidic chambers must be kept as uniform as possible, combining this characteristic with low power consumption (ideally below 1 W). With the simulated and experimentally outputted values of the heating system, its actuation, readout and power supply electronics system was developed and assembled, together with a capacitive keyboard, in a Printed Circuit Board (PCB) for portability.

This is the first reported study, to the best of the authors' knowledge, to fully study and optimize the best microheater geometry for temperature uniformization incorporated into an OoC device, that combines numerical simulation and experimental validation.

2. Methods

2.1. Numerical Simulations

The developed numerical model included a microheater area, defined as a resistive thin layer of aluminium, with a 110 nm thickness (to be similar to the thickness of the experimentally fabricated microheaters, as described in Section 2.2). Aluminium was selected due to its low cost, good linearity and easy microfabrication processes. In addition to this aluminium microheater, glass was considered as the substrate material, due to its low thermal conductivity, high electrical resistance and optical transparency in the visible spectral range, and air as the exterior domain, to assure heat dissipation through natural convection. The main properties of the glass substrate and the aluminium

Table 1
Main properties of glass and aluminium.

	Thermal Conductivity [W/(m·K)]	Heat capacity at constant pressure [J/(kg·K)]	Reference resistivity [Ω·m]	Resistivity temperature coefficient [1/K]	Reference temperature [K]	Density [kg/m^3]	Electrical conductivity [S/m]
Glass (Substrate)	1.38	703	n/a	n/a	n/a	2203	1.00E-14
Aluminium (Microheater)	237	904	3.44E-08	0.00429	293.15	2700	3.55E+ 07

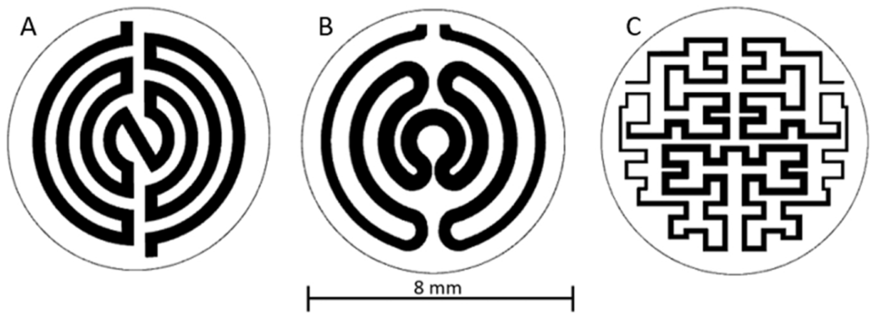

Fig. 2. Top view of the microheaters' geometries simulated in the COMSOL Multiphysics software: A - circular 1; B – circular 2; C - Hilbert. The circle outlining the microheaters represents the 8 mm diameter cell culture chamber.

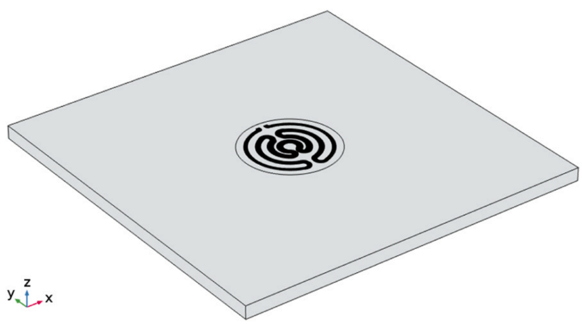

Fig. 3. Example of a complete geometry (in this example, geometry B is presented) comprised by a glass substrate (gray domain) and an aluminium microheater (black domain).

microheater used in the simulations, are presented in Table 1.

Regarding the studied geometries, three main configurations were designed and simulated in a 3D domain (Fig. 2). The first two configurations (circular 1 and circular 2, for simplification purposes, called A and B in Fig. 2, respectively) were based on a set of circular windings, which differ on the lines' width and on the filleting angles of the curvature turns. In particular, geometry A has a constant line width, and steep angles in the curvature regions, while geometry B has smoother curvatures and variable line width, with thinner lines on the outside and wider on the inside, to study the effect of this variation on the temperature distribution/uniformity. The third geometry (C), based on the Hilbert curves [25], resulted from an optimization of these curves, aiming the maximum space occupation, as represented in Fig. 2.

The geometries were designed according to existent dimensions' limitations, for further fabrication in CMEMS facilities (described in Section 2.2), including a limit of 50 µm as the minimum line width, available for the aluminium resistive filament, and a maximum 8 mm diameter to fit into the culture chamber (already optimized in cell studies). Firstly, using a computer aided design (CAD) software, the geometry was drawn. The microheater, with 110 nm thickness, was superposed above a 1.1 mm thick glass substrate, as represented in Fig. 3.

To perform the numerical simulations, the finite element methods (FEM) software, COMSOL Multiphysics, version 5.3, was used. To model the microheaters' performance, the electric currents and heat transfer modules were implemented, considering the multiphysics interfaces "Boundary electromagnetic heat source" and "Temperature coupling" to interconnect them.

The electric current interface is responsible for modelling an input current flowing in the microheater (110 nm thickness) which, through Joule effect, undergoes heating. For the electric current interface, the main governing equations are the following:

$$\nabla . J = Q_j \tag{1}$$

$$J = \sigma E + J_e \tag{2}$$

$$E = -\nabla V \tag{3}$$

where J is the current density (A/m^2), σ is the electrical conductivity (S/m), J_e is an externally generated current density (A/m^2), E is the electric field (V/m), Q_j is the external current source (A/m^3) and V (V) is the electric potential. Furthermore, it was defined a linearized resistivity for a temperature-dependent conductivity, described by:

$$\sigma = \frac{1}{\rho_0\left(1 + \alpha\left(T - T_{ref}\right)\right)} \tag{4}$$

where ρ_0 is the resistivity (Ω.m) at the reference temperature T_{ref} (°C), and α is the temperature coefficient of resistance (1/K), which describes how the resistivity varies with temperature T (°C). In the simulations, it was considered an aluminium resistivity (ρ_0) of 3.44×10^{-8} Ω·m, for a reference temperature (T_{ref}) of 20 °C, obtained by experimental measurements of a 110 nm thickness aluminium film, as well as a temperature coefficient of resistance (α) of 0.00429, selected from literature [26].

After modelling the Joule effect heating, the heat transfer model was used to simulate the heat propagation through the solid domains. For that purpose, the heat transfer module was considered. The heat transfer in solids is described by Eqs. 5 and 6:

$$\rho C_p\left(\frac{\partial T}{\partial t} + u_{trans}.\nabla T\right) + \nabla.(q + q_r) = -\alpha T : \frac{dS}{dt} + Q \tag{5}$$

$$Q_{Ted} = \alpha T : \frac{dS}{dt} \tag{6}$$

where ρ (kg/m^3) is the material density, Cp (J/(kg.K)) is the solid heat capacity at constant pressure, u_{trans} (m/s) represents the velocity field, T (°C) is the absolute temperature, q is the heat flux by conduction (W/m^2), q_r is the heat flux by radiation (W/m^2), S is the second Piola-Kirchhoff stress tensor and Q (W/m^3) is the heat source (or sink). The term Q_{ted} represents the thermoelastic damping, which accounts for the thermoelastic effects in solids.

For a steady state problem, the temperature does not change over time and, consequently, the time derivative terms disappear [27]. For the simulations, it was considered, as initial conditions, room temperature (20 °C) and 1 atm pressure.

The boundary conditions of the numerical problem included the definition of the microheaters' pads, by specifying current and ground terminals on opposite pads. Thermally, it was implemented an external natural convection with the exterior (air at room temperature) boundary condition, in all exterior boundaries. The heat losses were defined following Eq. 7, where q_0 is the heat flux density, T_{ext} is the external temperature, defined as room temperature, and h is the heat transfer coefficient [27].

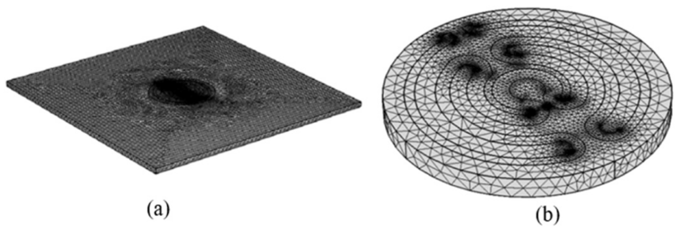

Fig. 4. Geometry B mesh: (a) View of the complete 3D mesh applied to the substrate and microheater. (b) Zoomed view of the meshing of the microheater region.

$$q_0 = h \times (T_{ext} - T) \tag{7}$$

The convective heat flux on the boundaries in contact with the fluid (air) was modelled as being proportional to the temperature difference across a fictitious thermal boundary layer. Furthermore, the heat transfer coefficient h is dependent on the Rayleigh (Ra_L) number, as presented in Eqs. 8, 9 and 10, where k represents the thermal conductivity and L is the characteristic length (defined as area/perimeter).

If $T > T_{ext}$, then:.

$$h = \begin{cases} \frac{k}{L} 0.54 Ra_L^{\frac{1}{4}} \text{ if } 10^4 \leq Ra_L \leq 10^7 & (8) \\ \frac{k}{L} 0.15 Ra_L^{\frac{1}{3}} \text{ if } 10^7 \leq Ra_L \leq 10^{11} & (9) \end{cases}$$

If $T \leq T_{ext}$, then:

$$h = \frac{k}{L} 0.27 Ra_L^{\frac{1}{4}} \text{if} 10^5 \leq Ra_L \leq 10^{10} \tag{10}$$

The Ra_L number (Eq. 11) depends on the structure geometry and material properties of the fluid, specifically the thermal conductivity k, dynamic viscosity μ, fluid density ρ, coefficient of thermal expansion α_p, heat capacity at constant pressure of the fluid Cp, surface temperature T and acceleration of gravity g.

$$Ra_L = \frac{g \alpha_p \rho^2 C_p |T - T_{ext}| L^3}{k \mu} \tag{11}$$

Regarding the mesh, each domain was meshed with an extremally fine grid, comprised by 59984, 124090 and 272372 tetrahedral elements for geometries A, B and C, respectively. The mesh independence studies performed for each geometry are summarized in supplementary material. As an example, Fig. 4 presents the tetrahedral-based mesh of geometry B.

For the simulations, a stationary study with a Multifrontal Massively Parallel Sparse direct solver (MUMPS) was considered, with a relative tolerance of 0.001 (the algorithm was solved for a maximum of 100 iterations). A parametric sweep of the applied current allowed to study the system for different input parameters.

When performing the numerical simulations, it was important to evaluate the performance of the microheaters in terms of their temperature uniformity and current consumption. A better temperature uniformity along all the microheater geometry allows for a better temperature control in the entire chamber and, consequently, provide the same temperature profile to all cells for their uniformly growth. Thus, in the numerical study, the main evaluated parameters were the energy consumption and the heat distribution, *i.e.*, the variation between the maximum and minimum temperature reached in each geometry, aiming for a temperature range between 35 °C and 45 °C, measured from the periphery of the chamber (8 mm diameter) up to its central area, as represented in Figs. 1 and 2.

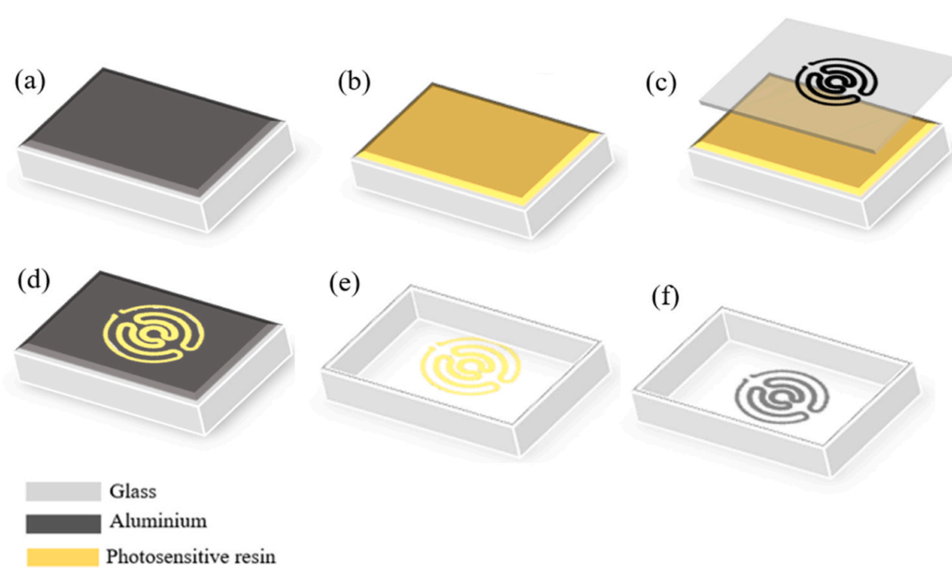

Fig. 5. Fabrication steps for the aluminium microheaters: (a) Deposition of an aluminium thin film on top of a glass substrate; (b) Deposition of AZ4562 photosensitive resin by spin-coating; (c) Photolithographic mask aligned over the photosensitive resin for UV exposure; (d) developing the photosensitive resin; (e) aluminium wet etching (f) removal of the remaining photosensitive resin.

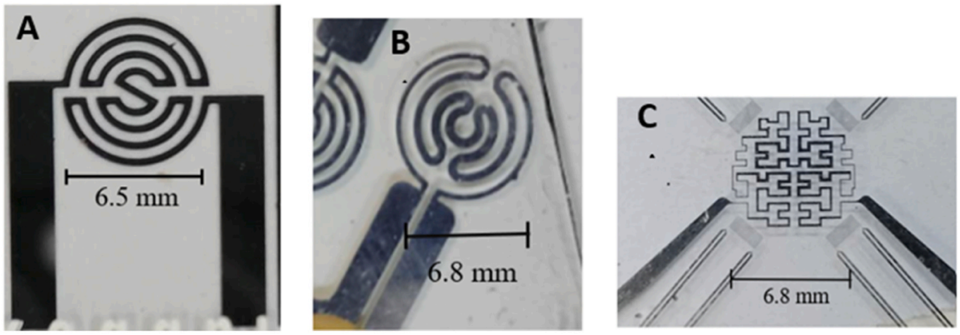

Fig. 6. Photographs of the fabricated aluminium microheaters.

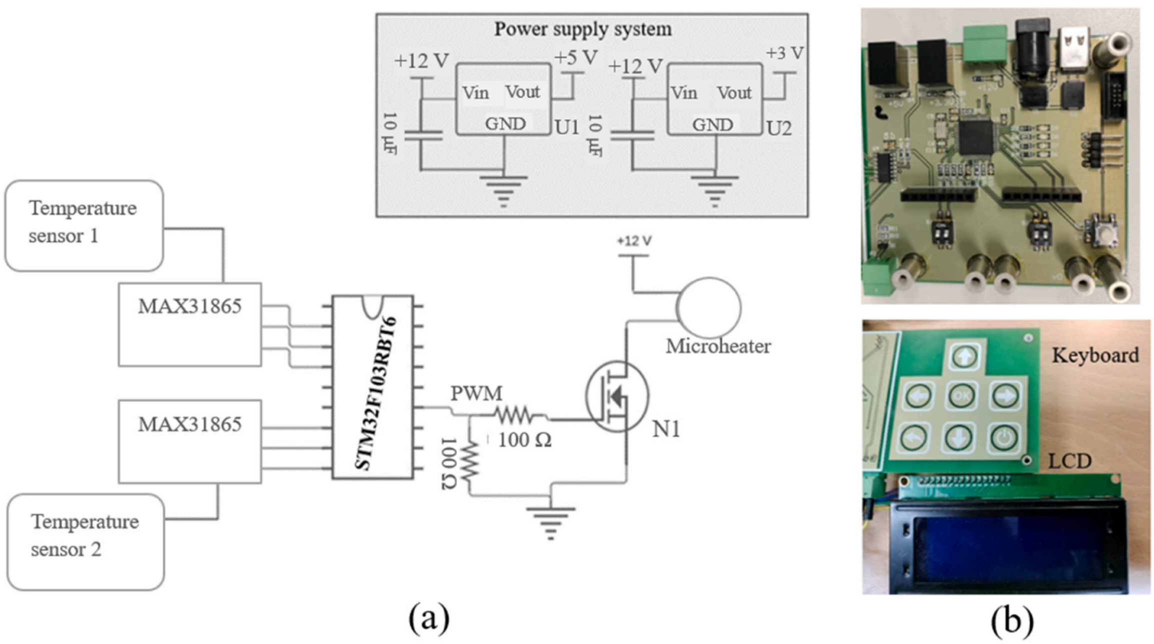

Fig. 7. (a) Schematic of the control and readout electronics for the microheaters' actuation and for the sensors' temperature measurements. (b) Photographs of the control electronics components, keyboard and LCD assembled in a PCB.

2.2. Fabrication process

In order to experimentally characterize the microheaters, the three proposed geometries (Fig. 2) were simultaneously fabricated in a single batch (to assure similar thickness). The aluminium thin film was obtained through physical vapor deposition (PVD) technologies and its patterning was performed using standard photolithography techniques and wet etching processes, using MicroChemicals AZ-family photoresist, developer and remover. The fabrication process began with the deposition of an aluminium thin film on a glass substrate (Fig. 5(a)). The thin film was deposited by thermal evaporation through electron beam (e-beam) with a thickness of 110 nm. The patterning process started with the spin-coating of the AZ 4562 photosensitive resin on top of the aluminium film using the Polos 200 equipment (Fig. 5(b)), with a rotation speed of 6000 rpm for 20 s. The photosensitive resin was cured on a hotplate at 100 °C for 10 min, followed by cooling to room temperature for 10 min. Then, the photosensitive resin was exposed to ultraviolet light for 3.5 min, using a photolithographic mask with the pattern of the geometry to be transferred (Fig. 5(c)). After the exposure step, the photosensitive resin was subjected to a development process using the AZ351-B developer diluted in distilled water, which removes the exposed resin, leaving only the patterned microheater geometry (Fig. 5(d)). Next, for the aluminium thin film wet etching process, a specific corrosive solution (Aluminium Etchant – Type A, Transene) was placed in a container where the sample was treated for approximately 30 s, followed by a wash with IPA (isopropyl alcohol) and drying with nitrogen flow (Fig. 5(e)). After removing the aluminium thin film, the samples were immersed in the AZ100 remover solution for 15 min, with magnetic agitation, for the remaining AZ4562 photosensitive resin removal, (Fig. 5(f)). Finally, it was checked whether the process was completed successfully, through visualization under the microscope and analysis of the thickness by profilometry. The three fabricated aluminium microheaters are presented in Fig. 6. The thickness of the deposited aluminium film was measured using a contact profilometer and it is presented in supplementary material.

2.3. Control electronics

The control electronics for the heating system comprises the control and readout electronics for the microheaters' actuation and for the sensors' temperature measurements (Fig. 7). It includes: (1) the power supply system that assures the stability of the input signals; (2) the Pulse Width Modulation (PWM)-based actuation system, for actuating the microheater programmed by a microcontroller and its firmware; (3) and two commercial temperature sensors [28], based on PT1000 RTDs, which signal is converted to digital by the Max31865 (Fig. 7(a)).

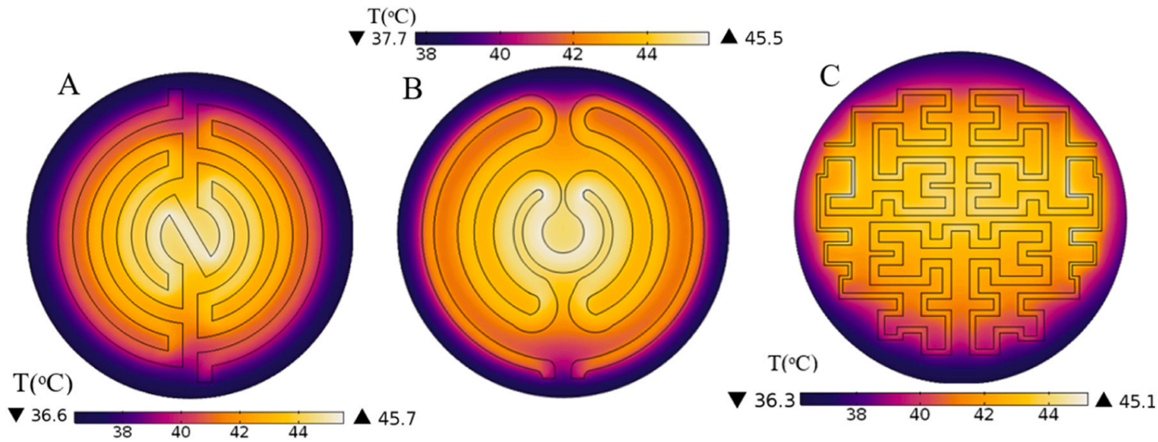

Fig. 8. Numerical heat distribution generated for each geometry (A – circular 1; B – circular 2; C - Hilbert), for an applied current of: (A) 53 mA; (B) 56 mA; (C) 26 mA.

Table 2
Simulated maximum, minimum, variation and average temperatures generated by the microheaters in the culture chamber using COMSOL Multiphysics software, aiming for target temperatures in the 35 °C to 45 °C range.

Geometry	Current (A)	Voltage (V)	Maximum temperature (°C)	Minimum temperature (°C)	Temperature variation (°C)	Average temperature (°C)
A	0.041	1.816	35.537	30.241	5.296	32.817
	0.043	1.914	37.032	31.182	5.850	34.027
	0.045	2.014	38.602	32.167	6.435	35.295
	0.047	2.116	40.249	33.195	7.054	36.624
	0.049	2.219	41.975	34.269	7.706	38.013
	0.051	2.324	43.782	35.389	8.393	39.466
	0.053	2.431	45.671	36.556	9.115	40.983
B	0.044	1.897	35.946	31.279	4.667	33.868
	0.046	1.994	37.367	32.246	5.121	35.087
	0.048	2.092	38.855	33.256	5.599	36.362
	0.050	2.191	40.410	34.308	6.102	37.693
	0.052	2.292	42.035	35.404	6.631	39.082
	0.054	2.394	43.731	36.545	7.186	40.53
	0.056	2.498	45.500	37.732	7.768	42.039
C	0.020	3.865	35.050	30.005	5.045	32.907
	0.021	4.080	36.529	30.942	5.587	34.153
	0.022	4.299	38.083	31.923	6.160	35.461
	0.023	4.521	39.716	32.947	6.769	36.832
	0.024	4.746	41.427	34.018	7.409	38.267
	0.025	4.976	43.220	35.134	8.086	39.768
	0.026	5.209	45.097	36.298	8.799	41.337

The current flow applied to the microheater is regulated by an N-type logic metal-oxide-semiconductor field-effect-transistor (MOSFET) (N1) that switches according to the PWM signal applied to its gate. The two platinum PT1000 RTDs are needed for controlling the microheater PWM signal. One was responsible for measuring the temperature on top of the microheater, and the other for measuring the temperature in an exterior reservoir (details of this configuration can be found in Section 3.3). These RTDs were selected as they present a wide operating range, between − 50 °C to 600 °C, being suitable for the needed operating temperature range, and have the required accuracy and sensitivity, also presenting high linear response and reduced dimensions [28]. Their output was read and amplified by the Adafruit PT1000 RTD Temperature Sensor Amplifier - MAX31865 board [29], routinely used for this purpose. The PWM signal applied to the microheater is controlled through the microcontroller by programming a proportional–integral–derivative (PID) controller algorithm. After reading the temperature sensor, the PID adjusts the error variable (comparison of measured and target temperatures) and, according to that value, changes the PWM duty cycle at the microcontroller output, thus triggering the MOSFET and so regulating the current flow for the microheater. When the desired temperature is reached, the error is zero and the duty cycle is also zero. In this case, the MOSFET is off and no current passes through the microheater. The programming of the three control terms of the PID, proportional gain (K_c), integral gain (K_i) and derivative gain (K_d) [30], were empirically and iteratively optimized, reaching 1.3, 1.05 and 1.1 for the K_c, K_i and K_D values, respectively.

The used microcontroller was the STM32F103RBT6, chosen due to its low cost and good resolution [31]. It also manages the display graphics and input interfaces. Additionally, for an easy visualization of the outputted parameters, a 20 × 4 Liquid Crystal Display (LCD) was used, since it allows, directly and in real time, monitoring the target temperature, the measured temperatures by the PT1000 sensors, and the PWM duty cycle applied to the actuation circuit. Also, to interact directly with the system, keeping a simpler design, a capacitive keyboard embedded in the PCB was developed. All components were assembled into a PCB, as demonstrated in Fig. 7(b), to connect with the microheater and OoC device for further testing.

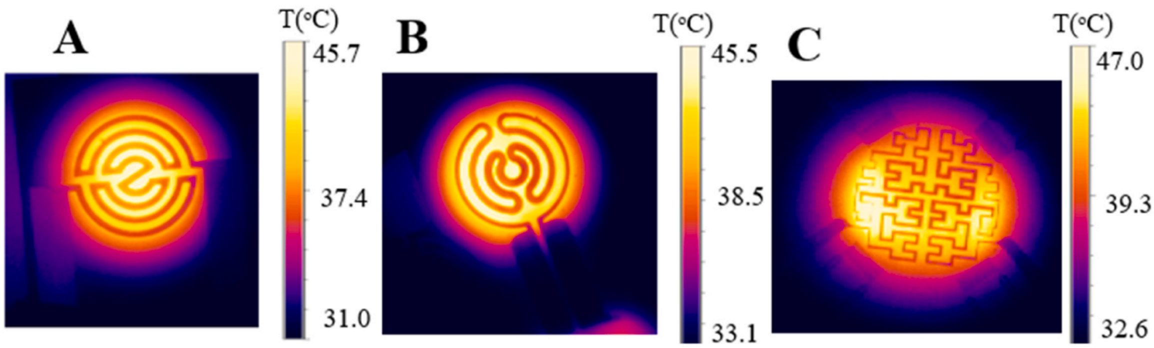

Fig. 9. Experimental measurements of the thermal radiation emitted by each geometry (A – circular 1; B – circular 2; C - Hilbert), using an IR camera, for an applied current of: (A) 80 mA; (B) 113 mA; (C) 50 mA.

Table 3
Experimentally measured maximum, minimum, variation and average temperatures generated by the microheaters, using an IR camera, aiming for target temperatures in the 35°C to 45 °C range.

Geometry	Current (A)	Voltage (V)	Maximum temperature (°C)	Minimum temperature (°C)	Temperature variation (°C)	Average temperature (°C)
A	0.058	5.341	35.30	28.81	6.49	31.69
	0.059	5.433	35.70	28.99	6.71	31.92
	0.061	5.621	36.60	29.15	7.45	32.34
	0.063	5.811	37.28	29.28	8.00	32.78
	0.065	6.025	38.10	29.44	8.66	33.28
	0.070	6.502	40.24	29.86	10.38	30.01
	0.075	7.013	43.11	30.51	12.60	36.04
	0.080	7.539	45.66	31.01	14.65	37.67
B	0.083	5.552	35.15	29.70	5.45	32.43
	0.084	5.619	35.49	29.86	5.63	32.66
	0.087	5.846	36.28	30.01	6.27	33.18
	0.089	5.981	37.08	30.41	6.67	33.68
	0.093	6.266	38.05	30.69	7.36	34.45
	0.100	6.781	40.19	31.52	8.67	35.99
	0.105	7.170	42.40	32.10	10.30	37.23
	0.113	7.782	45.50	33.17	12.33	39.28
C	0.036	5.267	35.10	28.19	6.91	31.74
	0.038	5.565	36.18	28.70	7.48	32.70
	0.040	5.886	38.12	29.44	8.68	33.94
	0.042	6.220	39.76	30.00	9.76	35.14
	0.044	6.543	41.50	30.54	10.96	36.34
	0.046	6.860	43.20	31.34	11.86	37.60
	0.048	7.200	45.28	32.00	13.28	38.90
	0.050	7.529	47.00	32.62	14.38	40.34

3. Results and discussion

3.1. Numerical results

The microheaters' heating distribution, generated by the designed geometries (presented in Fig. 2), was evaluated. Fig. 8 presents three numerical surface plots of the temperature distribution, one per geometry, when a specific current value was applied to each designed microheater, targeting the upper limits of the system temperature operating range, ~45 °C (for geometry A – 53 mA; for geometry B – 56 mA; for geometry C – 26 mA). Table 2 presents the complete numerical data, including input parameters (current and voltage) and temperature variations (maximum and minimum) in the domain, for the three geometries, for achieving the different target temperatures.

According to the numerical results reported in Table 2, geometry B was the best in terms of temperature uniformity (lower temperature variation) within the chamber area. This uniformity was defined by the difference between the maximum temperature (measured in the centre of the chamber) and the minimum temperature (on the outside, at a 4 mm radius distance from the centre, see Fig. 2), for each applied current. The geometry C, although it does not present a circular uniformity (it has an ellipsoid shape distribution, as observed in Fig. 8), consumes much less current than geometries A and B, to reach the same temperatures, due to its higher resistance, as a result of its thinnest filament width.

The obtained numerical results showed that the studied geometries fill the criteria to be used as microheaters, despite showing significant differences both in the temperature uniformity and distribution of heat. The simulation results also allowed to evaluate the power consumption needed for each type of microheater. Regarding this parameter, it is important to notice that the low power needed to supply the microheaters within the intended temperature range is critical, not only for long-term studies, but also for use in environments that lack external power (such as inside incubators).

3.2. Experimental characterization of the thermal radiation emitted by the microheaters

After the microheaters fabrication, and before the implementation of the control electronics, the thermal radiation emitted by each microheater geometry was experimentally characterized using an infrared (IR) camera (Optris PI 450 infrared) and a current source to supply the microheaters. The thermal radiation was measured for different input currents, aiming to reach the target temperatures (35 °C to 45 °C),

Table 4
Analytical, numerical and experimental characterization of the microheaters, regarding resistance and sensitivity.

	Resistance (Ω)			Sensitivity (°C/mA)	
Geometry	Analytical	Numerical	Experimental	Numerical	Experimental
A	44.30	45.05	90.10	0.844	0.468
B	40.78	43.84	65.40	0.796	0.339
C	180.23	196.68	138.8	1.674	0.868

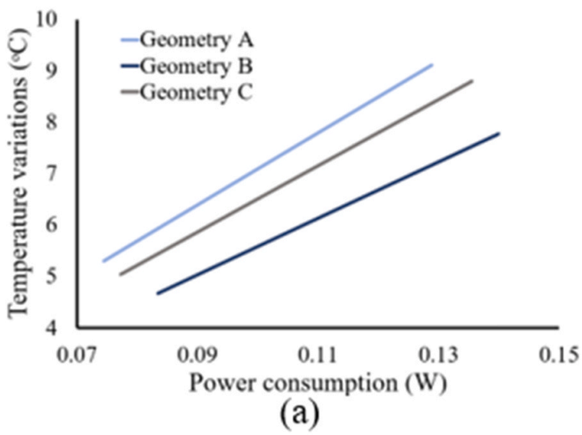

Fig. 10. Temperature variation within the culture chamber and correspondent power consumption for geometries A, B and C, for reaching the temperature range of 35 °C to 45 °C: (a) numerical simulation; (b) experimental tests using an IR camera.

similarly to what was numerically evaluated (Section 3.1). Fig. 9 presents examples of the measured temperature distribution in each of the geometries, when a specific current value was applied to each fabricated microheater, targeting the upper limits of the system temperature operating range, ~45 °C (geometry A – 80 mA; geometry B - 113 mA; geometry C - 50 mA). Table 3 presents the complete experimental data, measured with the IR camera, including input parameters (current and voltage) and temperature variations (maximum and minimum) in the microheater, for the three geometries, for achieving the different target temperatures.

The experimental results corroborate the numerical predictions (Section 3.1, Table 2). In particular, geometry B presents the lowest temperature variation and a slightly better uniformity of heat distribution than geometries A and C, while geometry C consumes lower currents than geometries A and B, to reach the same target temperature. As demonstrated in Fig. 9, geometry C does not present a perfect circular uniformity, in agreement with the simulation results, presenting a more distorted and ellipsoidal shape of the heat distribution.

The experimental results showed higher power consumptions than the predicted numerical values. In order to understand these differences, Table 4 presents a comparison between the analytical, numerical and experimental resistance and sensitivity of each microheater geometry. The analytical (theoretical) resistance of each microheater, R, was obtained by Eq. 7, where ρ is the resistivity of the material (ρ=3.44 × 10^{-8} Ω·m), L is the total length of the microheater, and S is the cross-sectional area.

$$R = \rho \times \frac{L}{S} \tag{12}$$

The analytical and numerical (outputted by COMSOL Multiphysics) resistances are very close, but significantly differ from the experimental resistance values, measured using a multimeter. These differences result from the presence, in the fabricated structures, of contact pads, copper wires and silver conductive paint, which were not considered in the analytical nor in the numerical calculus, but may impact the total resistance of the microheater devices. To confirm this hypothesis, it was also experimentally measured the resistance of a microheater (geometry B), without additional wiring or glue, and a resistance of 54 Ω was obtained, which is, as expected, closer to the analytical and numerical values.

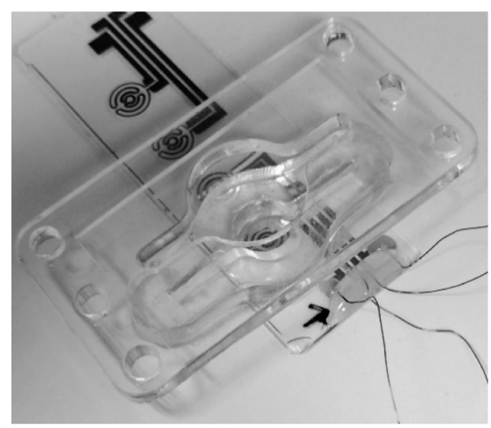

Fig. 11. PDMS microfluidic channel, with a fluid inlet and an outlet, comprising a culture chamber positioned and aligned on top of the aluminium microheater geometry B.

Regarding the achieved sensitivity, as demonstrated by Table 4, the sensitivities obtained by the numerical simulations and by the experimental tests were close. Geometry C, due to the smaller width of the aluminium filaments, presents a higher sensitivity than geometries A and B.

Furthermore, comparing the global temperature variations in the simulations and in the experimental tests, Fig. 10 shows a slightly higher temperature variation in the experimental tests. This difference may have been caused by the IR camera resolution and by external effects. Particularly, since the camera is positioned immediately above the microheaters, the IR waves emitted by the thermal camera are partially reflected by the metal and can influence the measured results. Additionally, the observed differences between the numerical and

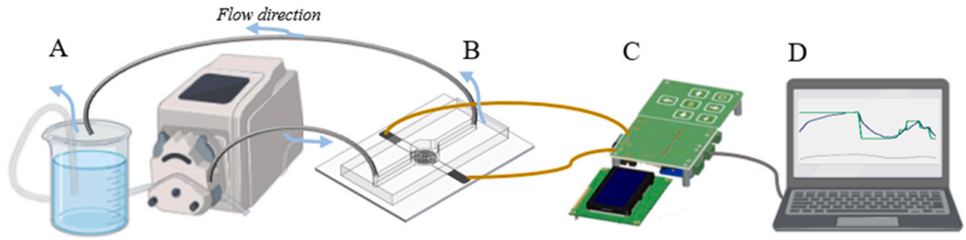

Fig. 12. Complete experimental setup composed by: (A) Pump and water reservoir; (B) PDMS microfluidic device and geometry B microheater; (C) control electronics assembled on a PCB; (D) computer for data acquisition and analysis.

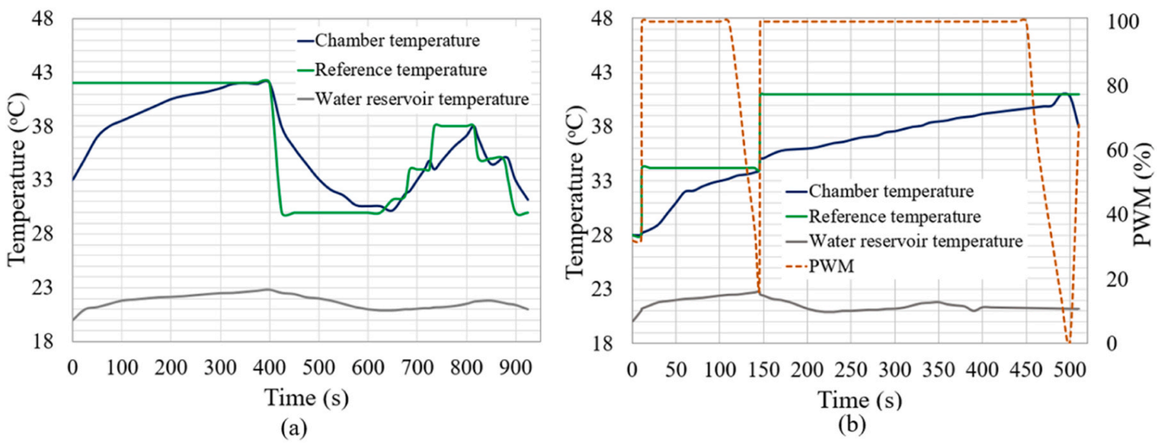

Fig. 13. (a) First experimental test with water cooling and heating, allowing the monitoring of the microheater (well region), reference, and water temperatures; (b) Second experimental test with visualization of the PWM duty cycle response, as well as the microheater (well region), reference, and water temperatures.

experimental power consumptions are justified by the different resistance values of the microheaters, previously discussed. Despite this, all geometries caused the heating of the domain, as expected, and all presented potential to be integrated into the OoC device. Nevertheless, due to the need to combine low power consumption with a good temperature uniformity in a circular area (area of the culture chamber), the circular-based layout presented in geometries A and B would be the preferred one. Additionally, between these two, the geometry B that comprises a variable line width is the one with the smallest temperature variation, *i.e.*, with the best thermal uniformity, combining good uniformity with low consumption.

3.3. Test of the control system integrated with the heating system

Finally, after characterization of the microheaters heat distribution, the complete heating system, including the control electronics (described in Section 2.3), was experimentally evaluated under a steady and dynamic water flow. For that purpose, it was used a PDMS microfluidic channel, comprising a chamber (positioned on top of the microheater), with an inlet and an outlet, as presented in Fig. 11. The microfluidic device was connected to a flow pumping system (Peristaltic Pump RP-QII, from BMT) for driving the fluid from the inlet to the outlet. It was defined a 2.5 V power supply for the fluidic pump, outputting a constant flow rate of 310 μL/s. A study of the flow rate effect was conducted in [32]. Briefly, as the flow rate increases, the temperature in the fluid chamber decreases due to heat dragging. Thus, for the same actuation conditions, the reached temperature will be higher and, therefore, the system will respond quickly and with lower consumption [32]. Experimental tests using cellular assays allowed to inferred that with that flow rate, 310 μL/s, the culture medium was able to reach the organ chamber providing cell nutrition. Therefore, this value was used for checking the proper functioning of the control system. These experimental assays were performed with the microheater with circular geometry B. The schematic of the fully autonomous and portable experimental setup is represented in Fig. 12.

In a first experimental test, as demonstrated in Fig. 13(a), it was defined an initial reference temperature of 43 ºC. When the chamber region (immediately on top of the aluminium microheater B) reached the reference temperature, measured by the PT1000, the reference temperature was changed to 30 ºC, and the microheater took about 250 s to cool down to the desired value. Then, the reference temperature was set to 38 ºC, taking about 212 s for heating the microheater up to this value. Simultaneously, the water reservoir temperature (Fig. 12(A)) was also monitored in real time, by the second PT1000, showing temperature variations inferior to 3 ºC during the entire experiment, as represented in Fig. 13 (a).

Then, a second phase experiment was implemented, to evaluate the PWM duty cycle response. In Fig. 13 (b), when the microheater temperature reached the reference temperature, the PWM duty cycle, as a system response, reacted very quickly. The system took 140 s to heat the liquid from 28 to 34 ºC, and an additional 360 s to reach 40 ºC.

The results show that the control system is able to adjust, in a short time, the microheater temperature, and thus, the culture chamber temperature. Furthermore, the system is able of controlling temperatures up to 42 °C, with resolution of less than 1 °C, reaching even a resolution of ~0.5 °C for temperatures below 38 °C. The system also operated properly for long periods of time (~12 h) without loss of performance or overheating.

4. Conclusion and future works

This paper presents the design, simulation, fabrication, and characterization of a miniaturized heating system, including microheaters based on aluminium thin film and control electronics, to be integrated into an OoC device. Numerical simulations were performed to study three microheater geometries, aiming for the most homogeneous temperature distribution possible, targeting the lowest power consumption. The simulations were performed for three geometries: two different circular-based geometries (one of them varying the width of aluminium line along the heater) and one Hilbert-based geometry. The last one, although presenting the lowest power consumption, did not present a circular heat distribution. The circular geometry with line width variation presented the best heat distribution, with lower temperature differences inside the culture chamber area (better for cells culture), also assuring low power consumption.

The experimental validation of the simulated results was performed using a thermal IR camera. The experimental results agreed with the numerical ones regarding the temperature distribution, showing the same ellipsoidal temperature distribution for the Hilbert-based geometry. The greatest difference recorded between numerical and experimental data was regarding the microheaters power consumption, as, experimentally, it was observed a higher power consumption for all geometries. Nevertheless, both numerical and experimental results allow to conclude that all geometries could be used as an effective heating system in an OoC device. The three geometries under analysis were able to achieve the target temperatures within a low power consumption (much lower than the 1 W established criteria), showing good (geometries A and B) and reasonable (geometry C) temperature uniformity, filling all the defined criteria.

The PID control electronics outputted a temperature variation of 0.05 ºC/s during cooling phases and a minimum of ~0.02 ºC/s during heating periods. Additionally, it could control the temperature up to 42 °C, with a resolution of 1 °C and, below 38 ºC, the system presents even a better resolution, reaching ~0.5 ºC, also being able to work properly for long periods of time (~12 h) without loss of performance.

The developed heating system disclosed to be suitable for integration into OoC devices, being able to control and ensure the target temperature required for cells' cultures. In future, thinner filament microheater geometries (particularly based on A and B designs) will be explored, optimizing even more their temperature control, keeping in mind the integration in OoC structures. Furthermore, instead of using commercial temperature PT1000 sensors, the implemented heating system will be integrated with microfabricated thin film RTDs (as reported in [5]), allowing for a better integration and optimization of the OoC device.

Declaration of Competing Interest

The authors declare the following financial interests/personal relationships which may be considered as potential competing interests: G. Minas reports financial support was provided by Fundação para a Ciência e a Tecnologia. G. Minas has patent #PCT/IB2022/051689 pending to UM and INL.

Data Availability

No data was used for the research described in the article.

Acknowledgements

This work has been supported by the project PTDC/EEI-EEE/2846/2021 and partially by 2022.02165. PTDC, through national funds (OE), within the scope of the Scientific Research and Technological Development Projects (IC&DT) program in all scientific domains (PTDC), through the Foundation for Science and Technology, I.P. (FCT, I.P). The authors also acknowledge the partial financial support within the R&D Unit Project Scope: UIDB/04436/2020. Gabriel M. Ferreira thanks FCT for his Ph.D. grant with reference 2022.10519. BD. Paulo Sousa, Vânia Pinto and Susana Catarino thank FCT for their contracts funding provided through 2021.01086. CEECIND, 2021.01087. CEECIND and 2020.00215. CEECIND, respectively. The authors would like to thank Dr. Paulo Mendes for access to the IR camera.

References

[1] A. Van Den Berg, C.L. Mummery, R. Passier, A.D. Van der Meer, Personalised organs-on-chips: functional testing for precision medicine, Lab Chip vol. 19 (2) (2019) 198–205, https://doi.org/10.1039/c8lc00827b.
[2] R.O. Rodrigues, P.C. Sousa, J. Gaspar, M. Bañobre-López, R. Lima, G. Minas, Organ-on-a-chip: a preclinical microfluidic platform for the progress of nanomedicine, Small vol. 16 (51) (2020), https://doi.org/10.1002/smll.202003517.
[3] I.M. Gonçalves, et al., Recent trends of biomaterials and biosensors for organ-on-chip platforms, Bioprinting vol. 26 (March) (2022), https://doi.org/10.1016/j.bprint.2022.e00202.
[4] K. Ronaldson-Bouchard, G. Vunjak-Novakovic, Organs-on-a-chip: a fast track for engineered human tissues in drug development, Cell Stem Cell vol. 22 (3) (2018) 310–324, https://doi.org/10.1016/j.stem.2018.02.011.
[5] P.J. Sousa, V.C. Pinto, V.H. Magalhães, R.O. Rodrigues, P.C. Sousa, G. Minas, Development of highly sensitive temperature microsensors for localized measurements, Appl. Sci. vol. 11 (9) (2021), https://doi.org/10.3390/app11093864.
[6] D.E. Ingber, Human organs-on-chips for disease modelling, drug development and personalized medicine, Nat. Rev. Genet. vol. 23 (8) (2022) 467–491, https://doi.org/10.1038/s41576-022-00466-9.
[7] I.M. Gonçalves, et al., Organ-on-a-chip platforms for drug screening and delivery in tumor cells: a systematic review, Cancers (Basel) vol. 14 (4) (2022) 1–25, https://doi.org/10.3390/cancers14040935.
[8] R.M. da Ponte, et al., Monolithic integration of a smart temperature sensor on a modular silicon-based organ-on-a-chip device (Jan.), Sens. Actuators A Phys. vol. 317 (2021), 112439, https://doi.org/10.1016/j.sna.2020.112439.
[9] Q. Wu, et al., Organ-on-a-chip: Recent breakthroughs and future prospects, Biomed. Eng. Online vol. 19 (1) (2020) 1–19, https://doi.org/10.1186/s12938-020-0752-0.
[10] F. Cantoni, G. Werr, L. Barbe, A.M. Porras, M. Tenje, A microfluidic chip carrier including temperature control and perfusion system for long-term cell imaging, HardwareX vol. 10 (2021), https://doi.org/10.1016/j.ohx.2021.e00245.
[11] M. Robert De Saint Vincent, Ŕ. Wunenburger, J.P. Delville, Laser switching and sorting for high speed digital microfluidics, Appl. Phys. Lett. vol. 92 (15) (2008) 1–4, https://doi.org/10.1063/1.2911913.
[12] P.H. Dannenberg, et al., Laser particle activated cell sorting in microfluidics, Lab Chip vol. 22 (12) (2022) 2343–2351, https://doi.org/10.1039/d2lc00235c.
[13] V. Miralles, A. Huerre, F. Malloggi, M.-C. Jullien, A review of heating and temperature control in microfluidic systems: techniques and applications (Jan.), Diagnostics vol. 3 (1) (2013) 33–67, https://doi.org/10.3390/diagnostics3010033.
[14] R.M. Guijt, A. Dodge, G.W.K. Van Dedem, N.F. De Rooij, E. Verpoorte, Chemical and physical processes for integrated temperature control in microfluidic devices, Lab Chip vol. 3 (1) (2003) 1–4, https://doi.org/10.1039/b210629a.
[15] T. Markovic, et al., Uniplanar microwave heater for digital microfluidics, 2017 1st IEEE MTT-S Int. Microw. Bio Conf. IMBioC 2017 (2017) 31–34, https://doi.org/10.1109/IMBIOC.2017.7965803.
[16] M. Sakr, S. Liu, A comprehensive review on applications of ohmic heating (OH), Renew. Sustain. Energy Rev. vol. 39 (November) (2014) 262–269, https://doi.org/10.1016/j.rser.2014.07.061.
[17] M. Afridi, C. Montgomery, Calibration and BIST vol. 116 (6) (2011) 827–838.
[18] T.M. Hsieh, C.H. Luo, F.C. Huang, J.H. Wang, L.J. Chien, G. Bin Lee, Enhancement of thermal uniformity for a microthermal cycler and its application for polymerase chain reaction, Sens. Actuators, B Chem. vol. 130 (2) (2008) 848–856, https://doi.org/10.1016/j.snb.2007.10.063.
[19] V.E. Papadopoulos, I.N. Kefala, G.D. Kaprou, A. Tserepi, G. Kokkoris, Modeling heat losses in microfluidic devices: The case of static chamber devices for DNA amplification (Mar.), Int. J. Heat. Mass Transf. vol. 184 (2022), 122011, https://doi.org/10.1016/j.ijheatmasstransfer.2021.122011.
[20] G.D. Kaprou, V. Papadopoulos, C.M. Loukas, G. Kokkoris, A. Tserepi, Towards PCB-based miniaturized thermocyclers for DNA amplification, Micromachines vol. 11 (3) (2020), https://doi.org/10.3390/mi11030258.
[21] O. Ibrahim, B. Jones, M. Hassab, M. Op De Beeck, Three-dimensional transient thermal analysis for a silicon PCR microreactor, Numer. Heat. Transf. Part A Appl. vol. 65 (11) (2014) 1069–1088, https://doi.org/10.1080/10407782.2013.851569.
[22] P. Skaltsounis, G. Kokkoris, T.G. Papaioannou, A. Tserepi, Closed-loop microreactor on PCB for ultra-fast DNA amplification: design and thermal validation (Jan.), Micromachines vol. 14 (1) (2023) 172, https://doi.org/10.3390/mi14010172.
[23] R.O. Rodrigues, et al., Multifunctional graphene-based magnetic nanocarriers for combined hyperthermia and dual stimuli-responsive drug delivery, Mater. Sci. Eng. C. vol. 93 (July) (2018) 206–217, https://doi.org/10.1016/j.msec.2018.07.060.
[24] V. Carvalho, M. Bañobre-López, G. Minas, S.F.C.F. Teixeira, R. Lima, R. O. Rodrigues, The integration of spheroids and organoids into organ-on-a-chip platforms for tumour research: a review, Bioprinting vol. 27 (July) (2022), https://doi.org/10.1016/j.bprint.2022.e00224.
[25] K.S.C. Karnati, S.R. Nagireddy, R.B. Mishra, A.M. Hussain, Design of micro-heaters inspired by space filling fractal curves, Proc. 2019 IEEE Reg. 10 Symp. TENSYMP 2019 vol. 7 (2019) 231–236, https://doi.org/10.1109/TENSYMP46218.2019.8971334.
[26] D.C. Giancoli, *Physics*, 4th ed. 1995.
[27] COMSOL Multiphysics, "Heat Transfer Module," © 1998–2018 Comsol, pp. 1–222, 2015, [Online]. Available: https://doc.comsol.com/5.4/doc/com.comsol.help.heat/HeatTransferModuleUsersGuide.pdf.
[28] C.W.A. Specialist, "Platinum Thin Film (PTF) Temperature Elements," pp. 1–9, 2020, [Online]. Available: https://www.te.com/commerce/DocumentDeliver

y/DDEController?Action=srchrtrv&DocNm=PTF-FAMILY&DocType=Data+Sheet&DocLang=English&DocFormat=pdf&PartCntxt=NB-PTCO-029.

[29] Maxim Integrated, "MAX31865 Datasheet," pp. 1–26, 2015, [Online]. Available: https://datasheets.maximintegrated.com/en/ds/MAX31865.pdf.

[30] K.H. Ang, G. Chong, Y. Li, "PID control system analysis, design, and technology, IEEE Trans. Control Syst. Technol. vol. 13 (4) (2005) 559–576, https://doi.org/10.1109/TCST.2005.847331.

[31] K.B. Flash, "STM32F103×8," no. March, pp. 1–117, 2022, [Online]. Available: https://pt.mouser.com/ProductDetail/STMicroelectronics/STM32F103RBT6?qs=bhCVus9SdFv12dJRZaBmJg%3D%3D.

[32] G.M. Ferreira, P.J. Sousa, V.C. Pinto, S.O. Catarino, P.C. Sousa, G. Minas, A numerical study of the heat distribution generated by a microheater in an organ-on-a-chip chamber, 2023 IEEE 7th Port. Meet. Bioeng. ENBENG 2023 (2023) 5–8, https://doi.org/10.1109/ENBENG58165.2023.10175328.

Gabriel M Ferreira completed his master's degree in Physics Engineering in February of 2022 by University of Minho, Portugal. In January of 2023, he started a PhD program in Electronic and Computer Engineering, specialization in Instrumentation and Electronic Microsystems also at university of Minho. His research interests include numerical simulators, microfabrication, and microelectronic systems for biomedical applications.

Filipe M. Azevedo is graduated in Industrial Electronics and Computers Engineering from University of Minho (2022) where he developed a heating microsystem integrated in organ-on-a-chip devices. His main research areas are on Medical Electronics, focusing on development of sensors and actuators for integration in microfluidic devices, for medical diagnostics.

Paulo J. Sousa is graduated in Biotechnology Engineering with master's in Micro/Nano Technologies. In 2017, he received the PhD degree in Biomedical Engineering from the University of Minho, Portugal. He was awarded with an Junior Researcher Contract - Stimulus of Scientific Employment, Individual Support (CEECIND), reference 2021.01086. CEECIND - 4th Edition (2021), funded by Fundação para a Ciência e Tecnologia (FCT). His current research interests include the development of sensors and actuators for organ-on-a-chip devices. His main research areas are on biomedical microsystems, focused on lab-on-a-chip devices, microfluidics, microfabrication techniques, biosensors, immunosensors, micro-pressure sensors, optical detection and organ-on-a-chip.

Vânia C. Pinto is graduated in Biotechnology Engineering with master's in Micro/Nano Technologies. In 2017, she received the PhD degree in Biomedical Engineering from the University of Minho, Portugal. In 2021, she was awarded with a FCT competitive 6-year junior research contract at CMEMS and is an Invited Assistant Professor, lecturing in the areas of biosensors, microtechnologies and bionanotechnologies. Her current research interests include the development of biomedical microsystems, focused on microfluidics, microfabrication, immunosensors and lab-on-chip (LOC) devices.

Susana O. Catarino is an Assistant Researcher in the Microelectromechanical Systems Research Unit - CMEMS and LABBELS Associate Laboratory, at University of Minho, and, since 2016, a Visiting Assistant Professor at the Department of Industrial Electronics in the same university. She finished the PhD in Biomedical Engineering in 2014 and the M.Sc. Degree in Biomedical Engineering (specialization in Medical Electronics) in 2009. Her main research area is Biomedical Engineering, focusing on numerical simulation and development of optical and acoustic transducers for integration in microfluidic devices, for medical applications.

Patrícia C. Sousa is a Research Engineer at the Integrated Micro and Nanotechnologies research group of the International Iberian Nanotechnology Laboratory (INL). She obtained her PhD in Chemical and Biological Engineering in 2010, from the Faculty of Engineering, University of Porto, with research studies on microfluidics and rheology. Currently, her main research interests focus on the micro- and nano-fabrication level, with emphasis to nanoimprint, and also to the application level with emphasis to biosensors.

Graça Minas received the Ph.D. degree in 2004 from University of Minho, Portugal. Her thesis work was in cooperation with the Laboratory for Electronic Instrumentation, Delft University of Technology, The Netherlands, and dealt with lab-on-a chips for biological fluids analysis. Presently, she is an Associate Professor with Habilitation at the Department of Industrial Electronics and a researcher at CMEMS (Center for MicroElectroMechanical Systems), both at University of Minho, where she is involved in biomedical microdevices research. Her research is basically focussed on lab-on-a-chip devices and organ-on-a-chip with on-chip integration of electronic circuits, optical filters, sensors, biosensors and microactuators.